Ultra-thin BPH nanosheets with exceptional water adsorption properties

Edwin Clatworthy, Rémy Guillet-Nicolas, Philippe Boullay, Michael Badawi, Yann Foucaud, Eddy Dib, Nicolas Barrier, Arnold Paecklar, Maxime Debost, Sajjad Ghojavand, et al.

Ultra-Thin BPH Nanosheets with Exceptional Water Adsorption Properties

Edwin B. Clatworthy,[a] Rémy Guillet-Nicolas,[a] Philippe Boullay,[b] Michael Badawi,[c] Yann Foucaud,[d] Eddy Dib,[a] Nicolas Barrier,[b] Arnold A. Paecklar,[b] Maxime Debost,[a,b] Sajjad Ghojavand,[a] Jean-Pierre Gilson,[a] Izabel Medeiros-Costa,[e] and Svetlana Mintova[a]**

[a] Normandie Université, ENSICAEN, UNICAEN, CNRS, Laboratoire Catalyse et Spectrochimie (LCS), 14050 Caen, France

[b] Normandie Université, ENSICAEN, UNICAEN, CNRS Laboratoire de Cristallographie et Sciences des Matériaux (CRISMAT), 14050, Caen, France

[c] Université de Lorraine, CNRS, Laboratoire Lorrain de Chimie Moléculaire (L2CM), F-57000 Metz, France

[d] Université de Lorraine, CNRS, GeoRessources, F-54000 Nancy, France

[e] TotalEnergies OneTech Belgium, Feluy, B-7181 Seneffe, Belgium

ABSTRACT: The synthesis of ultra-thin BPH zeolite nanosheets from an aluminosilicate colloidal suspension using exclusively inorganic structure directing agents under mild conditions is reported. The improved synthesis yields nanosheets of 4–7 nm and a Si/Al ratio of 1.5; combined 3D electron diffraction and DFT calculations reveal the spatial distribution of extra-framework cations throughout the microporous structure. The ultra-thin BPH nanosheets exhibit high and regular inter-sheet mesoporosity, and substantially improved thermal stability. The notable mesoporosity bestows exceptional water adsorption behavior typically unseen for zeolites; the as-prepared material consists of up to 49% adsorbed H_2O by weight, and adsorbs up to 32 wt% H_2O at 90% relative humidity. ^2H MAS NMR spectroscopy identifies different types of O^2H environments ascribed to silanol species exhibiting two motion behaviors. H_2O sorption analysis demonstrates reproducible behavior over multiple cycles and low temperature regeneration, making the ultra-thin BPH nanosheets attractive candidates for gas drying and membrane applications.

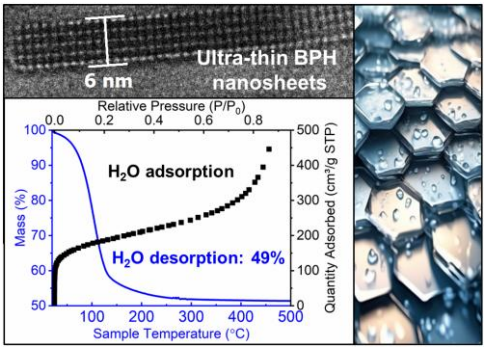

Synthetic zeolites are fundamental to the production of petrochemicals, gases, and consumer products, upon which modern society depends.[1, 2] As the increasing deployment of renewable energy displaces fossil-derived electricity and fuels, the product slate of refineries will need to adjust to lower fuel and higher chemical production while simultaneously managing the integration of renewable biomass-derived feedstocks, CO_2 valorization, and process electrification.[3-6] In addition to the aforementioned scenarios, synthetic zeolites also remain a source of interest for biomedical and environmental remediation applications.[7, 8] In light of the variety of applications presented, the ability to intelligently design a zeolite with a specific set of properties which are essential for a particular role is of fundamental importance.[9-11] However, because of the intertwined nature of various synthesis parameters, the simultaneous tailoring of the morphological, physical and chemical properties of zeolite crystals to obtain a desired outcome is immensely challenging.[12-15] In particular, the hydrophilic properties of zeolites will be influenced not only by the framework topology, but also the framework composition (Si/Al ratio) and extra-framework population.[16] Analogously, the topology and structural composition (metal centers, linkers) are important controls for tuning the hydrophilicity of other crystalline microporous materials such as metal-organic frameworks.[17-20] In comparison, the hydrophilicity of gel composites can be tuned by incorporated polymers and hygroscopic salts,[21] whereas carbons can be tuned through their surface functional groups.[22]

Here we describe the synthesis and characterization of a new BPH nanozeolite exhibiting ultra-thin nanosheet morphology, which confer upon it exceptional adsorption abilities and two silanol environments showing a kind of ordered motion.[23-25] Our earlier procedure for BPH nanosheets, described as thin-BPH (T-BPH) nanosheets

served as the basis of the synthetic strategy, whereby the optimization of the synthesis lies within the tuning of the

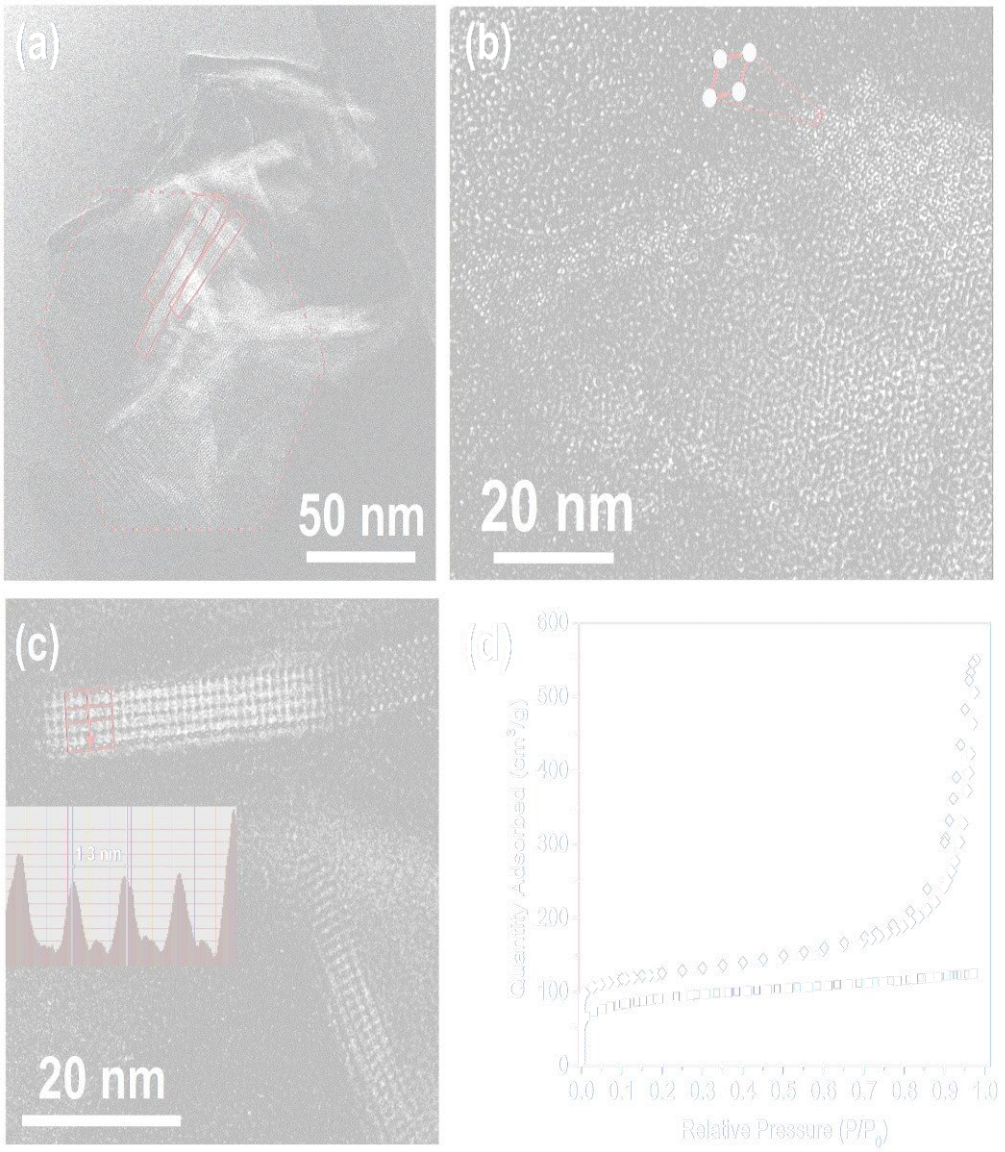

Figure 1. (a) HR Low magnification bright field TEM images showing analysis of the UT-BPH nanosheets. Depending on their crystallographic orientation, the nanosheets appear either as sheets (dashed blue line) or as bundles of rods (solid blue lines). (b) HR TEM image of fragments of nanosheets with the c-axis oriented out-of-plane. The lattice parameter corresponding to the unit highlighted in blue is about 1.3 nm. (c) HR TEM image of two isolated sheets (~ 6 nm thick) corresponding to fragments of nanosheets with the c-axis oriented in-plane. Inset: the line profile perpendicular to the thickness of the upper sheet allows an estimation of the c lattice parameter of 1.3 nm. (d) N_2 (diamonds) and Ar (squares) adsorption (full) and desorption (empty) isotherms recorded at −196 °C and −186 °C respectively.

ratio of the alkali metal cations (Na^+, K^+ and Cs^+) while maintaining a similar level of alkalinity in order to sustain a high rate of nucleation.[26] Essentially, the Na^+ content was decreased while the K^+ and Cs^+ content was increased. X-ray powder diffraction (XRPD) analysis of the zeolite product confirms the BPH framework structure and indicates the formation of nanosheets with small crystalline domains due to the low intensity and broadening of the reflections, principally the (001) reflection at 6.15° 2θ (Figure S1). Le Bail refinements of the XRPD pattern reveal that the ultra-thin BPH (UT-BPH) nanosheets possess a smaller lattice parameter and unit cell volume than that of the T-BPH nanosheets (Figure S2, Table S1). This is consistent with the elemental analysis results whereby the UT-BPH nanosheets have an increased Si/Al ratio of 1.5 in comparison to the T-BPH nanosheets with an Si/Al ratio of 1.3 (Table S2). High resolution transmission electron microscopy (HR TEM) clearly reveals the ultra-thin morphology of the nanosheets, primarily between 4–7 nm thick (Figures 1a–c). This represents a significant reduction compared to the thickness of the T-BPH nanosheets (up to 19 nm). The high crystallinity of UT-BPH nanosheets enables lattice parameters, consistent with those obtained from PXRD, to be estimated. This confirms that the observed rod or sheet bundles are in fact UT-BPH nanosheets oriented differently. The morphology is comparable to ultra-thin FER nanosheets and nanocrystalline like PST-

12,[27, 28] yet no organic molecules are required to achieve the ultra-thin morphology of the UT-BPH nanosheets.

In situ variable temperature XRPD analysis in air shows a dramatic improvement in the thermal stability of the UT-BPH nanosheets, up to ~500 °C (Figure S3), consistent with the increased Si/Al ratio determined by elemental analysis. The intensity of the most intense Bragg reflection at 7.6° 2θ increases until 200 °C, which is associated with the removal of physisorbed water; above 200 °C the intensity decreases. There is no evidence to suggest a change in the morphology of the UT-BPH nanosheets during the variable temperature treatment as there are no signs of recrystallisation or interzeolite conversion from the *in situ* XRPD results. Analysis of the UT-BPH nanosheets by ^{29}Si MAS NMR spectroscopy reveals a spectrum with at least five peaks, similar to that of the T-BPH nanosheets. The Si/Al ratio obtained after the deconvolution of the ^{29}Si spectrum is equal to 1.3, note that the five peaks observed were assigned to different Al coordination of the Si nuclei (Figure S4). ^{27}Al MAS NMR spectroscopy shows a band at 63 ppm indicative that all of the aluminum atoms in the UT-BPH nanosheets are tetrahedrally coordinated (Figure S5). The textural properties, determined by N_2 sorption at −196 °C and Ar sorption at −186 °C, are presented in Figures 1d, S6–7, and Table S3. The specific surface area was determined using the updated Rouquerol criteria in the BETSI software (Figures S8–11).[29] While the micropore volume is comparable to the T-BPH nanosheets, the UT-BPH nanosheets possess high external surface area and exhibit significant interparticle, or inter-sheet, mesoporosity (P/P_0 >0.8) similar to what has been observed for ultra-small (10 nm) FAU nanocrystals.[30] This interparticle mesoporosity is related to the reduced thickness of the nanosheets in the [001] direction, increasing the surface area to volume ratio.

Structural information about the location of the extra-framework cations was first obtained from continuous rotation 3D electron diffraction performed on isolated UT-BPH nanosheets (see Supporting Information for details).[31, 32] From the electrostatic potential density maps obtained from *ab initio* structure determination (Figure 2), three extra-framework cation positions are identified: EF1 within the side-pocket of the 12 membered-ring channel, EF2 within the 8 membered-ring formed from the interlinking of *t-afo* units in the [001] direction, and EF3 within the trigonal *t-afo* cage. Using this model, subsequent structure refinement (kinematical approximation) confirms the presence of extra-framework cations for these three positions. The precise chemical identity of each cation could not be determined (see Supporting Information for details), however, the proposed locations of the extra-framework cations are consistent with earlier analyses of beryllophosphate-H and Linde Q.[33, 34] Hence, DFT calculations were performed on several possible structural configurations to get insights on the location of the extra-framework cations (Table S4, Figure S12). First, calculations confirmed that the potassium cations are located in the 8 membered-ring formed from the interlinking of *t-afo* units while the sodium cations are located in the trigonal *t-afo* cage. Some (1 out of 3 per formula unit) potassium cations can the substitute sodium cations. Moreover, the cesium cations are located in the 12 membered-ring channels, but some of them (1 out of 4 per formula unit) can substitute potassium cations in the 8 membered-rings. The substitutions are equal in terms of energy between all possible sites. The obtained all-electron

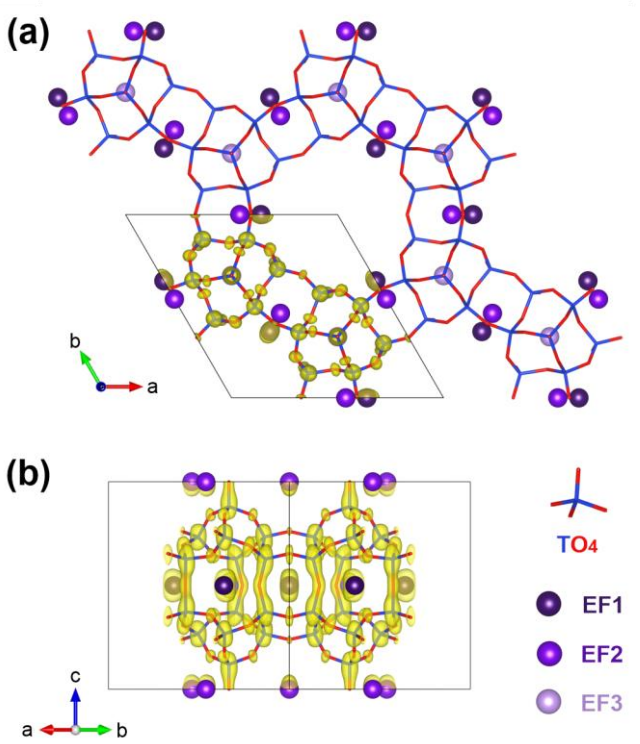

Figure 2. Electrostatic potential map (isosurfaces in yellow ovoid-like shapes) obtained from the *ab initio* structure solution using UT-BPH nanosheets 3D ED data sets, and projected along the directions (a) [001] and (b) [110] of the unit cell. The proposed extra-framework (EF) cation positions (purple spheres) and BPH framework structure (TO_4 tetrahedra) are overlaid.

densities satisfactorily correspond to the experimental electron density maps (Figure S13), based on the formula unit determined from ICP-MS measurements.

Surprisingly, thermogravimetric (TG) analysis of the UT-BPH nanosheets reveals an incredibly large mass loss event centered at ~100 °C. This is ascribed to the removal of physisorbed H_2O at the external surface and within the micropores; the total mass loss of the sample was 49% (Figure 3a). Asymmetry of the first derivative curve above ~150 °C is attributed to desorption of a portion of microporous H_2O which is strongly coordinated, but corresponds to 5.4% of the total loss of mass only. *In situ* FTIR analysis of the UT-BPH nanosheets confirms that the majority of adsorbed H_2O can be removed below 100 °C (Figure 3b). After remaining under high vacuum at 25 °C overnight the sample still retains a significant amount of water evidenced by the intense broad band between ~3700–2500 cm^{-1} representative of H-bonding, and the sharper H_2O bending band at 1661 cm^{-1}. A band at 1417 cm^{-1} is associated with a negligible amount of carbonate species and completely disappears at 350 °C. The shift of the silanol bands are indicative of isolated species (Figure S13);[35] weak proton donor and acceptor species are pre-

sent below 100 °C due to the significant amount of physisorbed H_2O molecules.

Volumetric equilibrium H_2O adsorption analysis of the UT-BPH nanosheets reveals that adsorption within the micropores ($P/P_0 \leq 0.1$) and on the external surface, or inter-sheet mesopores ($0.6 \leq P/P_0 \leq 0.9$), accounts for ~40% each

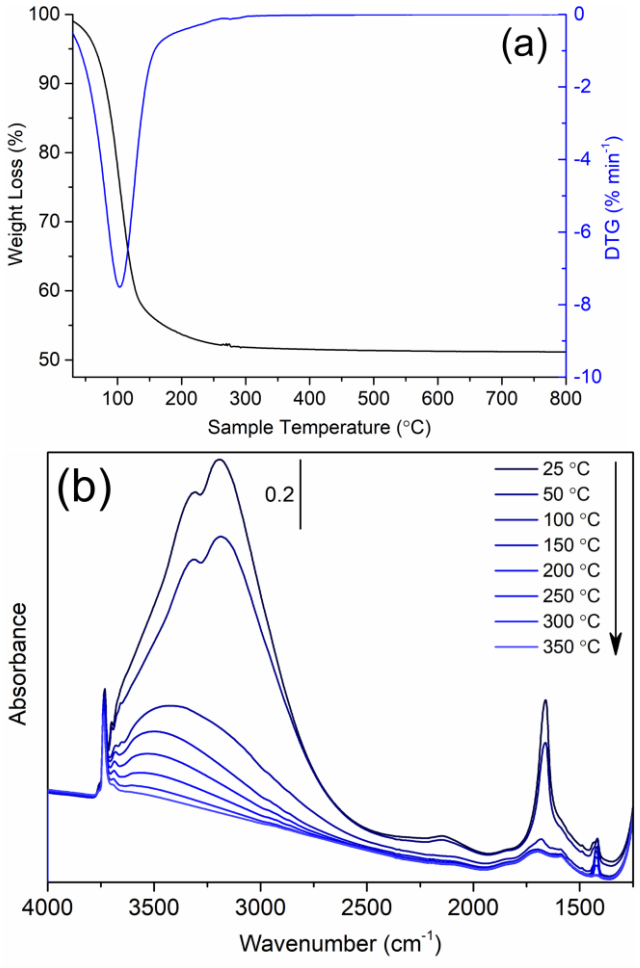

Figure 3. (a) Weight loss (black) and first derivative (blue) curves obtained from the thermogravimetric analysis of the UT-BPH nanosheets. (b) *In situ* FTIR spectra of the UT-BPH nanosheets subjected to dehydration from 25 °C to 350 °C.

of the total adsorption amount (Figures 4 and S14). This permits the UT-BPH nanosheets to have significant working capacity in both low and high humidity environments, and greater uptake of H_2O than the T-BPH nanosheets due to the reduced sheet thickness, *i.e.* greater adsorption of H_2O on the external surface. Cyclic gravimetric equilibrium H_2O adsorption experiments presented in Figure 4b demonstrates the stability of the zeolite over multiple adsorption and desorption steps, and that the majority of adsorbed H_2O (70% of the total adsorption capacity) can be removed at mild temperatures under inert atmosphere. The relatively low temperature required to remove the majority of the H_2O from the UT-BPH nanosheets is attributed to the significant amount of the H_2O being located on the external surface of the zeolite, and the presence of Cs^+ extra-framework cations which have a lower enthalpy of hydration compared to Na^+ and K^+.[36-38]

To further understand the relationship between the external surface and the adsorption behavior of the ultra-thin nanosheets, Hg porosimetry analysis was performed on both the T-BPH and UT-BPH nanosheets (Figures S15–17). Both zeolite samples exhibit compaction at the beginning of the analysis followed by two intrusion events corresponding to the porosity between the agglomerates of nanosheets, or macropores, and the inter-sheet mesoporosity (Figure S15). Interestingly, the UT-BPH nanosheets exhibit a clearly defined demarcation between the filling of the porosity between the nanosheet agglomerates (~4000 nm), smaller macropores (~300 nm) and the beginning of the inter-sheet mesoporosity (~50 nm). Analysis of the mesopore region shows that the UT-BPH nanosheets exhibit both a higher absolute value (0.78 *vs* 0.72 mL/g) and more regular porosity compared to the T-BPH nanosheets. Cycling extrusion and intrusion experiments shows that both zeolite samples exhibit an expected reproducible hysteresis, however, the UT-BPH nanosheets appear to retain their mesoporous structure while the T-BPH nanosheets lose part of their mesoporosity due to an irreversible/inelastic alteration of the 'macrostructure' (Figures S16, S17). In combination with the zeolite chemical properties, we propose that the highly regular interparticle mesoporosity of the UT-BPH nanosheets permits the exceptionally high amount of surface-adsorbed H_2O. This is reflected by the approximate doubling of the adsorbed amount of H_2O between $0.7 > P/P_0 > 0.9$ for the UT-BPH nanosheets compared to the T-BPH nanosheets (Figures 4a, S14).

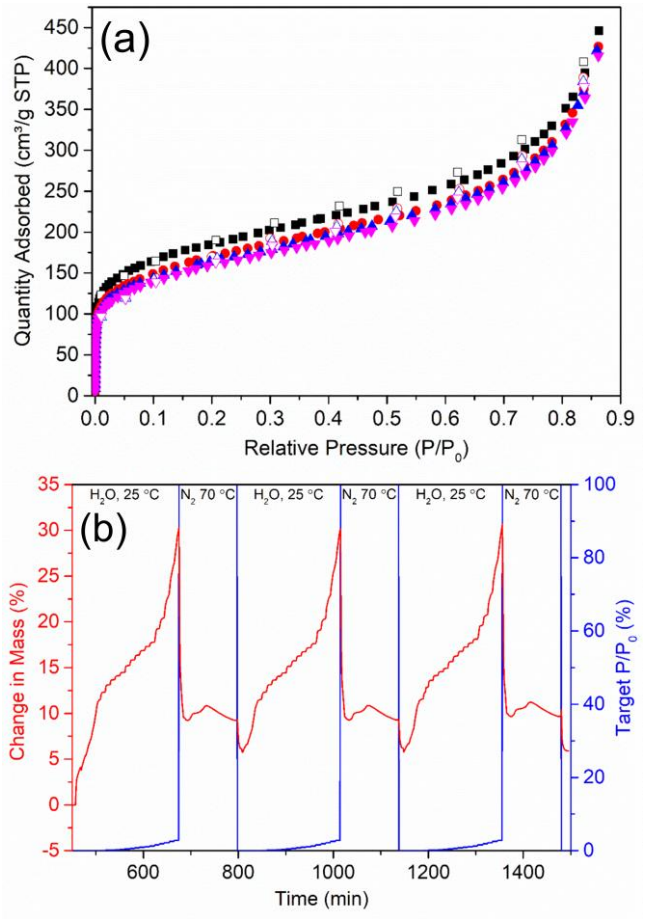

Figure 4. Water sorption analysis of the UT-BPH nanohseets. (a) Volumetric equilibrium H_2O adsorption isotherms (full symbols) and desorption isotherms (empty symbols), pre-treated (350 °C, high vacuum) and measured (25 °C) multiple times; first (black squares), second (red circles), third (blue triangles), fourth (magenta inverted triangles). (b) Gravimetric equilibrium H_2O adsorption analysis at 25 °C, and desorption analysis at 70 °C under N_2.

The high content of framework aluminum and large number of accessible extra-framework cations confers hydrophilic behavior to the zeolite framework and within the pore network, respectively. While extra-framework cations located near the channel apertures may help facilitate adsorption near the zeolite surface, the presence of silanols on the external surface (Figure S13) also provides adsorption sites for H_2O. To obtain more information about the silanol species, the UT-BPH nanosheets were investigated by deuterium (^2H) MAS NMR spectroscopy. The use of deuterium in NMR analysis has been employed previously to probe O–H site geometry and dynamics in both organic and inorganic substances,[39] including zeolites, whereby distinctions between different O–H environments (Brønsted acid sites and silanols) can be made.[40, 41] Combined with MAS, the first order quadrupole broadening is partially averaged out. This permits the determination of the isotropic chemical shift of different ^2H environments from the spinning side band pattern.[42-44] The experimental ^2H spectra and corresponding fits are presented in Figure 5. Analysis of the spectrum identified two main ^2H (silanol, SiOH) environments with a 4 ppm difference. The relative proportions of the two environments were 80% and 20%; environment 1 possessing a C_Q = 140 kHz, η_Q = 0.8 and δ_{iso} = 2 ppm, and environment 2 possessing a C_Q = 230 kHz, η_Q = 0.1 and δ_{iso} = 7 ppm. Similar to our observations from ^2H MAS NMR spectroscopic analysis of Na-X zeolite, the motion of O^{2}H environments of the UT-BPH nanosheets appear well ordered due to the unique shape of the spectrum, representative of a unique electric field gradient. A possible explanation for the two observed environments may be the location of silanols at either the sheet faces or edges. This is supported in principle by the by *in situ* FTIR observations of an intense silanol band which

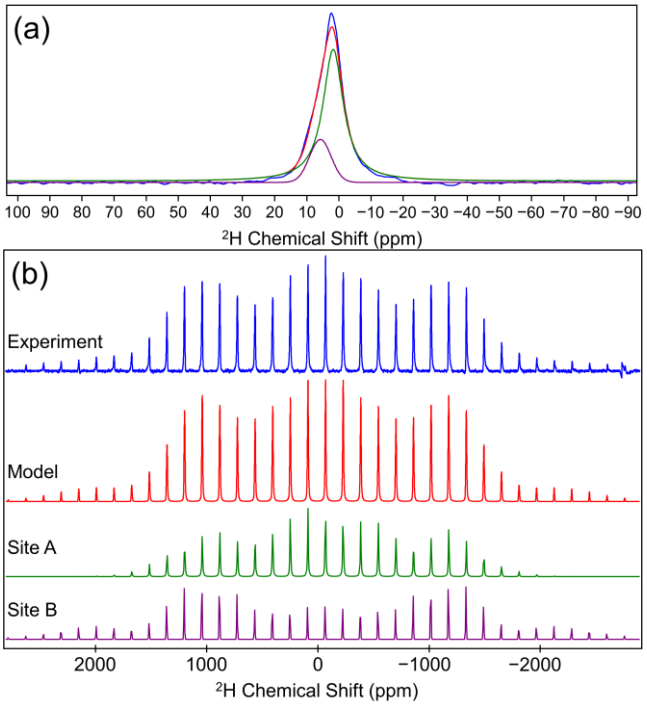

Figure 5. ^2H MAS NMR analysis of the deuterated UT-BPH nanosheets: (a) deconvolution of the central spinning side band, and (b) experimental and fitted spectra.

appears to be composed of multiple species. However, we have previously described how varying the extra-framework Cs^+/K^+ cation ratio can alter the population of silanol groups in nano-sized chabazite.[45] We may speculate that the spatial distributions of the Cs^+ and K^+ extra-framework cations are also likely to wield some influence over the environment and motion of the silanol species of the UT-BPH nanosheets.[45]

While zeolites will continue to play fundamental roles in the petrochemical industry and consumer products, the energy transition and advances in biomedical applications will require researchers to push the limits of zeolite synthesis into unknown territory, in which nanozeolites will be a key feature. In summary, here we have demonstrated the synthesis of UT-BPH zeolite nanosheets with a Si/Al ratio of 1.5 and improved thermal stability over its predecessor, T-BPH nanosheets. The combined ultra-thin morphology and high inter-particle mesoporosity, multi-cationic composition, and hydrophilic nature permit the UT-BPH nanosheets to exhibit exceptional water adsorp-

tion behavior, with an adsorption capacity of 49 wt.% and facile regeneration. This makes them not only interesting candidates for membrane fabrication, but other applications requiring materials with combined thermal and chemical stability, rapid diffusion properties, and high surface areas to facilitate molecule and catalyst loading.

ASSOCIATED CONTENT

Supporting Information. Materials, synthetic and experimental method descriptions, ambient and variable temperature XRPD analyses, Le Bail profile refinement results, ^{29}Si and ^{27}Al MAS NMR spectra, N_2, Ar and H_2O sorption analysis results, DFT calculations and structural model, *in situ* FTIR spectra, Hg porosimetry analysis results. This material is available free of charge via the Internet at http://pubs.acs.org.

AUTHOR INFORMATION

Corresponding Author

*Edwin B. Clatworthy – Normandie Université, ENSICAEN, UNICAEN, CNRS, Laboratoire Catalyse et Spectrochimie (LCS), 14050 Caen, France; orcid.org/0000-0002-7204-2213 edwin.clatworthy@ensicaen.fr

*Svetlana Mintova – Normandie Université, ENSICAEN, UNICAEN, CNRS, Laboratoire Catalyse et Spectrochimie (LCS), 14050 Caen, France; orcid.org/0000-0002-0738-5244 svetlana.mintova@ensicaen.fr

Author Contributions

The manuscript was written through contributions of all authors. All authors have given approval to the final version of the manuscript.

ACKNOWLEDGMENT

The authors wish to thank Dr Stéphanie Gascoin for her assistance in recording XRPD patterns for Le Bail profile refinement. The theoretical modelling work was granted access to the HPC resources of TGCC under the allocation 2023-A0140810433 made by GENCI. Co-funded by the European Union (ERC, ZEOLIghT, 101054004). Views and opinions expressed are however those of the author(s) only and do not necessarily reflect those of the European Union or the European Research Council. Neither the European Union nor the granting authority can be held responsible for them. This project has received funding from the Region of Normandy via the Label of Excellence for the Centre of Zeolites and Nanoporous Materials and the Industrial Chair Project "ECOGAS" supported by the Region of Normandy and TotalEnergies.

REFERENCES

(1) Vermeiren, W.; Gilson, J.-P. Impact of Zeolites on the Petroleum and Petrochemical Industry. *Top. Catal.* **2009**, *52*, 1131-1161.

(2) Masters, A. F.; Maschmeyer, T. Zeolites–From curiosity to cornerstone. *Microporous Mesoporous Mater.* **2011**, *142*, 423-438.

(3) Ennaert, T.; Van Aelst, J.; Dijkmans, J.; De Clercq, R.; Schutyser, W.; Dusselier, M.; Verboekend, D.; Sels, B. F. Potential and challenges of zeolite chemistry in the catalytic conversion of biomass. *Chem. Soc. Rev.* **2016**, *45*, 584-611.

(4) Nesterenko, N.; Medeiros-Costa, I. C.; Clatworthy, E. B.; Cruchade, H.; Konnov, S. V.; Dath, J.-P.; Gilson, J.-P.; Mintova, S. Methane-to-chemicals: a pathway to decarbonization. *Natl. Sci. Rev.* **2023**, *10*, nwad116.

(5) Serrano, D. P.; Centi, G.; Diddams, P. A.; Čejka, J. Outlooks for zeolite catalysts in a low-carbon scenario. *Catal. Today* **2024**, *426*, 114365.

(6) Velty, A.; Corma, A. Advanced zeolite and ordered mesoporous silica-based catalysts for the conversion of CO_2 to chemicals and fuels. *Chem. Soc. Rev.* **2023**, *52*, 1773-1946.

(7) Matusiak, J.; Przekora, A.; Franus, W. Zeolites and zeolite imidazolate frameworks on a quest to obtain the ideal biomaterial for biomedical applications: A review. *Mater. Today* **2023**.

(8) Williams, C. D. Application of zeolites to environmental remediation. In *Urban Pollution: Science and Management*, Charlesworth, S. M., Booth, C. A. Eds.; Vol. 1; Wiley-Blackwell, 2018; pp 249-258.

(9) Dusselier, M.; Davis, M. E. Small-pore zeolites: synthesis and catalysis. *Chem. Rev.* **2018**, *118*, 5265-5329.

(10) Palčić, A.; Valtchev, V. Analysis and control of acid sites in zeolites. *Appl. Catal. A* **2020**, *606*, 117795.

(11) Pérez-Botella, E.; Valencia, S.; Rey, F. Zeolites in adsorption processes: State of the art and future prospects. *Chem. Rev.* **2022**, *122*, 17647-17695.

(12) Cundy, C. S.; Cox, P. A. The hydrothermal synthesis of zeolites: Precursors, intermediates and reaction mechanism. *Microporous Mesoporous Mater.* **2005**, *82*, 1-78.

(13) Mintova, S.; Gilson, J.-P.; Valtchev, V. Advances in nanosized zeolites. *Nanoscale* **2013**, *5*, 6693-6703.

(14) Deneyer, A.; Ke, Q.; Devos, J.; Dusselier, M. Zeolite synthesis under nonconventional conditions: reagents, reactors, and modi operandi. *Chem. Mater.* **2020**, *32*, 4884-4919.

(15) Mallette, A. J.; Seo, S.; Rimer, J. D. Synthesis strategies and design principles for nanosized and hierarchical zeolites. *Nat. Synth.* **2022**, *1*, 521-534.

(16) Ng, E.-P.; Mintova, S. Nanoporous materials with enhanced hydrophilicity and high water sorption capacity. *Microporous Mesoporous Mater.* **2008**, *114*, 1-26.

(17) Wright, A. M.; Rieth, A. J.; Yang, S.; Wang, E. N.; Dincă, M. Precise control of pore hydrophilicity enabled by post-synthetic cation exchange in metal–organic frameworks. *Chem. Sci.* **2018**, *9*, 3856-3859.

(18) Schlüsener, C.; Xhinovci, M.; Ernst, S.-J.; Schmitz, A.; Tannert, N.; Janiak, C. Solid-Solution Mixed-Linker Synthesis of Isoreticular Al-Based MOFs for an Easy Hydrophilicity Tuning in Water-Sorption Heat Transformations. *Chem. Mater.* **2019**, *31*, 4051-4062.

(19) Kalmutzki, M. J.; Diercks, C. S.; Yaghi, O. M. Metal–Organic Frameworks for Water Harvesting from Air. *Adv. Mater.* **2018**, *30*, 1704304.

(20) Xu, W.; Yaghi, O. M. Metal–Organic Frameworks for Water Harvesting from Air, Anywhere, Anytime. *ACS Cent. Sci.* **2020**, *6*, 1348-1354.

(21) Zhou, X.; Lu, H.; Zhao, F.; Yu, G. Atmospheric Water Harvesting: A Review of Material and Structural Designs. *ACS Materials Letters* **2020**, *2*, 671-684.

(22) Legrand, U.; Klassen, D.; Watson, S.; Aufoujal, A.; Nisol, B.; Boudreault, R.; Waters, K. E.; Meunier, J.-L.; Girard-Lauriault, P.-L.; Wertheimer, M. R. Nanoporous Sponges as Carbon-Based Sorbents for Atmospheric Water Generation. *Ind. Eng. Chem. Res.* **2021**, *60*, 12923-12933.

(23) Mintova, S.; Clatworthy, E.; Debost, M.; Ghojavand, S.; Kumar, P.; Pugnet, V.; Nesterenko, N. Aluminosilicate zeolite with high adsorption capacity for water. WO2024153604A1, 2024.

(24) Mintova, S.; Clatworthy, E.; Gilson, J.-P.; Guillet-Nicolas, R.; Kumar, P.; Pugnet, V.; Nesterenko, N. Method of drying gas and regenerating adsorbent. WO2024153620A1, 2024.

(25) Mintova, S.; Clatworthy, E.; Gilson, J.-P.; Guillet-Nicolas, R.; Kumar, P.; Pugnet, V.; Nesterenko, N. Use of an aluminosilicate zeolite for separating CO_2. WO2024153611A1, 2024.

(26) Clatworthy, E. B.; Debost, M.; Barrier, N.; Gascoin, S.; Boullay, P.; Vicente, A.; Gilson, J.-P.; Dath, J.-P.; Nesterenko, N.; Mintova, S. Room-Temperature Synthesis of BPH Zeolite Nanosheets Free of Organic Template with Enhanced Stability for Gas Separations. *ACS Appl. Nano Mater.* **2020**, *4*, 24-28.

(27) Xu, H.; Chen, W.; Zhang, G.; Wei, P.; Wu, Q.; Zhu, L.; Meng, X.; Li, X.; Fei, J.; Han, S. Ultrathin nanosheets of aluminosilicate FER zeolites synthesized in the presence of a sole small organic ammonium. *J. Mater. Chem. A* **2019**, *7*, 16671-16676.

(28) Park, M. B.; Ahn, S. H.; Ahn, N. H.; Hong, S. B. Charge density mismatch synthesis of MEI-and BPH-type zeolites in the TEA^{+}–TMA^{+}–Li^{+}–Sr^{2+} mixed-structure-directing agent system. *Chem. Commun.* **2015**, *51*, 3671-3673.

(29) Osterrieth, J. W.; Rampersad, J.; Madden, D.; Rampal, N.; Skoric, L.; Connolly, B.; Allendorf, M. D.; Stavila, V.; Snider, J. L.; Ameloot, R. How reproducible are surface areas calculated from the BET equation? *Adv. Mater.* **2022**, *34*, 2201502.

(30) Awala, H.; Gilson, J.-P.; Retoux, R.; Boullay, P.; Goupil, J.-M.; Valtchev, V.; Mintova, S. Template-free nanosized faujasite-type zeolites. *Nat. Mater.* **2015**, *14*, 447-451.

(31) Nederlof, I.; van Genderen, E.; Li, Y.-W.; Abrahams, J. P. A Medipix quantum area detector allows rotation electron diffraction data collection from submicrometre three-dimensional protein crystals. *Acta Crystallogr. Sect. D. Biol. Crystallogr.* **2013**, *69*, 1223-1230.

(32) Gemmi, M.; Mugnaioli, E.; Gorelik, T. E.; Kolb, U.; Palatinus, L.; Boullay, P.; Hovmöller, S.; Abrahams, J. P. 3D electron diffraction: the nanocrystallography revolution. *ACS Cent. Sci.* **2019**, *5*, 1315-1329.

(33) Harvey, G.; Baerlocher, C.; Wroblewski, T. Structure solution and Rietveld refinement of beryllophosphate-H zeolite. *Z. Kristallogr. - Cryst. Mater.* **1992**, *201*, 113-124.

(34) Andries, K.; Bosmans, H.; Grobet, P. The crystal structure of zeolite Linde Q: A proposal based on powder X-ray diffraction and ^{27}Al and ^{29}Si MAS nmr spectroscopy. *Zeolites* **1991**, *11*, 124-131.

(35) Dib, E.; Costa, I. M.; Vayssilov, G. N.; Aleksandrov, H. A.; Mintova, S. Complex H-bonded silanol network in zeolites revealed by IR and NMR spectroscopy combined with DFT calculations. *J. Mater. Chem. A* **2021**, *9*, 27347-27352.

(36) Smith, D. W. Ionic hydration enthalpies. *J. Chem. Educ.* **1977**, *54*, 540.

(37) Dzhigit, O.; Kiselev, A.; Mikos, K.; Muttik, G.; Rahmanova, T. Heats of adsorption of water vapour on X-zeolites containing Li^{+}, Na^{+}, K^{+}, Rb^{+}, and Cs^{+} cations. *Trans. Faraday Society* **1971**, *67*, 458-467.

(38) Joshi, U.; Joshi, P.; Tamhankar, S.; Joshi, V.; Idage, B.; Joshi, V.; Shiralkar, V. Influence of the size of extraframework monovalent cations in X-type zeolite on their thermal behavior. *Thermochim. Acta* **2002**, *387*, 121-130.

(39) Sternberg, U.; Brunner, E. The influence of short-range geometry on the chemical shift of protons in hydrogen bonds. *J. Magn. Reson., Ser A* **1994**, *108*, 142-150.

(40) Kobe, J.; Gluszak, T.; Dumesic, J.; Root, T. Deuterium NMR Characterization of Broested Acid Sites and Silanol Species in Zeolites. *J. Phys. Chem.* **1995**, *99*, 5485-5491.

(41) Ernst, H.; Freude, D.; Wolf, I. Multinuclear solid-state NMR studies of Brønsted sites in zeolites. *Chem. Phys. Lett.* **1993**, *212*, 588-596.

(42) Ackerman, J.; Eckman, R.; Pines, A. Experimental results on deuterium NMR in the solid state by magic angle sample spinning. *Chem. Phys.* **1979**, *42*, 423-428.

(43) Laws, D. D.; Bitter, H. M. L.; Jerschow, A. Solid-state NMR spectroscopic methods in chemistry. *Angew. Chem. Int. Ed.* **2002**, *41*, 3096-3129.

(44) Dib, E.; Clatworthy, E. B.; Lakiss, L.; Ruaux, V.; Mintova, S. Hydroxyl environments in zeolites probed by deuterium solid-state MAS NMR combined with IR spectroscopy. *Inorg. Chem. Front.* **2022**, *9*, 2964-2968.

(45) Ghojavand, S.; Dib, E.; Rey, J.; Daouli, A.; Clatworthy, E. B.; Bazin, P.; Ruaux, V.; Badawi, M.; Mintova, S. Interplay between alkali-metal cations and silanol sites in nanosized CHA zeolite and implications for CO_2 adsorption. *Commun. Chem.* **2023**, *6*, 134.